Energy & Environmental Science

ROYAL SOCIETY OF CHEMISTRY

PAPER

View Article Online
View Journal

Cite this: DOI: 10.1039/d6ee01515h

Strain-mediated grain-boundary reconstruction unlocks high near-room-temperature thermoelectric performance in Mg_3Sb_2-based alloys

Gang Wu, †[a] Airan Li, †[a] Harish Subramania,[a] Xinzhi Wu, [a] Longquan Wang,[a] Jiankang Li,[ab] Fei Frank Yun[a] and Takao Mori *[ab]

Achieving high thermoelectric efficiency across a wide temperature range, including near room temperature, within a single Mg_3Sb_2-based material remains challenging, because the microstructures that favor low-temperature charge transport often conflict with those required for phonon suppression. Here, we demonstrate that subtle lattice perturbations can steer strain-mediated grain-boundary spectrum reconstruction in Mg_3Sb_2-based systems. The grain-boundary spectrum reconfiguration markedly weakens grain-boundary potential barriers and alleviates carrier scattering by raising the fraction of coherent twin boundaries, thereby restoring the power factor near room temperature. Within the same processing window, the multifunctional $CuGaTe_2$ additive also undergoes composition-partitioning, yielding a uniformly dispersed *in situ* Cu–Ga-rich intermetallic phase together with point defects. The resulting multi-length-scale defect landscape provides broadband phonon scattering and suppresses lattice thermal conductivity toward the diffusion limit. Consequently, the optimized alloy delivers an exceptional ZT_{ave} of 1.3 at ΔT = 250 K, exceeding that of state-of-the-art n-type Bi_2Te_3, while maintaining a ZT_{ave} of 1.59 from 300–723 K with a peak ZT of 2.08 at 623 K. Device demonstrations further validate the material-level advantages with 8% for the assembled TE module (ΔT = 300 K) and 12.4% for a single-leg generator (ΔT = 400 K). These results indicate that grain-boundary spectrum reconstruction can serve as an effective route to improve near-room-temperature performance and help narrow the performance gap between the near-room- and mid-temperature regimes in n-type Mg_3Sb_2 for broader waste-heat recovery.

Received 6th March 2026,
Accepted 27th April 2026

DOI: 10.1039/d6ee01515h

rsc.li/ees

Broader context

Recovering low-grade waste heat is important for improving energy efficiency, yet many thermoelectric materials still suffer from a mismatch between near-room-temperature and mid-temperature performance. N-type Mg_3Sb_2-based materials are particularly promising because of their cost and mid-temperature potential, but their near-room-temperature transport is often limited by grain-boundary scattering. This work shows that a multifunctional $CuGaTe_2$ additive can be used to simultaneously reconfigure the grain-boundary spectrum and generate *in situ* Cu–Ga-rich precipitates, thereby improving electrical transport near room temperature while retaining strong phonon scattering at higher temperatures. The result broadens the temperature-window performance. More generally, these results suggest that coordinated regulation of the grain-boundary character and precipitate architecture can be an effective route for designing thermoelectric materials that operate efficiently over practical temperature gradients relevant to waste-heat harvesting.

Introduction

During fossil fuel energy conversion, about two-thirds of the generated energy cannot be utilized efficiently and is dissipated as thermal losses, especially within the room- to intermediate-temperature range, where conventional heat engines are incapable of efficiently harvesting this heat energy.[1–4] Thermoelectric (TE) materials, which are capable of directly converting heat

[a] *Research Center for Materials Nanoarchitectonics (MANA), National Institute for Materials Science (NIMS), Tsukuba, 305-0044, Japan. E-mail: MORI.Takao@nims.go.jp*
[b] *Graduate School of Pure and Applied Science, University of Tsukuba, 1-1-1 Tennodai, Tsukuba, Ibaraki 305-8671, Japan*
† These authors contributed equally to this work.

into electricity *via* the Seebeck effect without generating any pollutants, have aroused widespread interest. The dimensionless figure of merit (ZT) of materials dictates the TE conversion efficiency (η), where ZT is governed by three interrelated parameters: electrical conductivity (σ), Seebeck coefficient (S) and thermal conductivity (κ_{tot}). Integrating high power factor ($S^2\sigma$) with low thermal conductivity is essential for achieving high ZT.[5,6] However, designing TE materials that orchestrate a synergistic optimization between electronic and phonon transport across a broad temperature range remains a formidable challenge.[7,8]

Recently, $Mg_3(Sb, Bi)_2$-based materials have emerged as compelling candidates for commercial applications, combining earth-abundant constituents with excellent n-type performance and strong potential for scalable commercialization.[9–15] The electronic band alignment and lattice dynamics of $Mg_3(Sb, Bi)_2$ can be effectively tuned by adjusting the composition of either Sb or Bi.[16,17] Normally, the Bi/Sb ratio not only tunes the electronic transport but also dictates the intrinsic trade-off between performance and stability in $Mg_3(Sb, Bi)_2$ materials.[18–20] Bi-rich compositions, such as $Mg_3Bi_{1.5}Sb_{0.5}$, exhibit excellent near-room-temperature performance due to their narrow band gap and low density-of-states effective mass, but its higher formation energy and severe bipolar effect above 400 K undermine the stability and TE performance.[21,22] In contrast, Sb-rich compositions like $Mg_3Sb_{1.5}Bi_{0.5}$ deliver high performance in the mid-temperature range, while their TE performance near room temperature remains suboptimal.[23,24] For practical TE devices, achieving high and stable efficiency across the full temperature span is crucial.[25,26] Bridging this performance gap, by extending the high efficiency of Sb-rich $Mg_3(Sb, Bi)_2$ toward the low-temperature regime, is essential to push forward its application.

The relatively low power factor of Mg_3Sb_2-based materials near room temperature mainly arises from carrier mobility degradation caused by strong grain boundary (GB) scattering,[27–29] which reduces the average power factor in the near-room-temperature range. Therefore, mitigating GB scattering is key to enhancing their near-room-temperature thermoelectric performance. According to Seto's model,[30] mobility can be expressed as,

$$\mu_{GB} = Le\left(\frac{1}{2\pi m^* k_B T}\right)^{\frac{1}{2}} \exp\left(\frac{-E_b}{k_B T}\right) \quad (1)$$

where L, e, m^*, k_B and E_b represent the grain size, electron charge, density-of-states effective mass, Boltzmann constant and potential barrier height, respectively. Thus, carrier mobility is primarily governed by the grain size and potential barrier height. Traditionally, the approaches of enlarging grain size and thereby reducing boundary density, such as long-time annealing or liquid-phase sintering, enhance the carrier mobility.[31–34] However, this way may adversely affect κ_{lat}. Directly reducing the potential barrier height, E_b, seems to be a more attractive strategy. Additionally, the potential barrier height can be expressed as[35]

$$E_b = \frac{e^2 Q_t^2}{8N\varepsilon_{st}} \quad (2)$$

where Q_t, N and ε_{st} are the trapping states, concentration of impurity atoms and static dielectric permittivity. The barrier at high-angle grain boundaries is typically three to five times larger than that at low-angle boundaries because of a larger number of trapping states.[36,37] Conversely, twin boundaries (TBs) are characterized by coherent atomic arrangements and minimal electronic potential perturbation, which are regarded as electron transparent yet phonon opaque interfaces.[38–40] Thus, increasing the fraction of TBs while reducing high-angle grain boundaries to reduce the potential barrier height serves as an effective approach to reconcile electrical and thermal transport.

In addition to GB scattering, a lower κ_{lat} is also a crucial pathway for achieving high performance. Although the Mg_3Sb_2-based material exhibits an intrinsically low κ_{lat} due to its complex bonding, it still remains significantly higher than the theoretical minimum predicted by the phonon diffusion limit, leaving substantial room for further thermal optimization. A widely used route is nanoscale structural modulation through controlling defect or second-phase size, spatial dispersion and interface coherency to broaden phonon scattering over a wide spectral window.[41–43] However, the central obstruction is to introduce such phonon-blocking architectures without undermining electrical transport. Sustaining high thermoelectric performance across wide temperature ranges especially for a near-room region in the Mg_3Sb_2 system remains a central challenge. Addressing this limitation is vital for enabling low-cost and scalable thermoelectric power generation.

In this work, we show that $CuGaTe_2$-enabled strain-mediated grain-boundary spectrum reconstruction provides a distinct route to improve near-room-temperature performance while retaining competitive mid-temperature behaviour in the Mg_3Sb_2-based system. Rather than relying on grain coarsening to simply reduce boundary density, which may compromise phonon transport or processing control, the additive introduces localized lattice perturbations that reconfigure the grain-boundary spectrum, raising the fraction of coherent twin boundaries and reducing the high-barrier boundaries. This reconstruction effectively mitigates grain boundary scattering and lowers E_b, thereby restoring the power factor near room temperature. Notably, during ball milling and subsequent sintering, the $CuGaTe_2$ additive undergoes partial interdiffusion and local redistribution of Cu, Ga and Te, which generates processing-induced compositional fluctuations. Under Te-deficient conditions, these redistributed species subsequently partition, giving rise to *in situ* Cu–Ga-rich precipitates and associated point-defect structures, serving as broad-scale phonon-scattering centers and reducing κ_{lat} to 0.49 W m^{-1} K^{-1} at room temperature. A schematic representation of the mechanism is displayed in Fig. 1a. As a result, the Mg_3Sb_2-based material achieves a superior average ZT (ZT_{ave}) of 1.3 at ΔT = 250 K, surpassing most reported n-type Bi_2Te_3 and rivalling Mg_3Bi_2-based alloys. Moreover, a ZT_{ave} of 1.59 is maintained across 300–723 K, demonstrating superiority in the mid-temperature

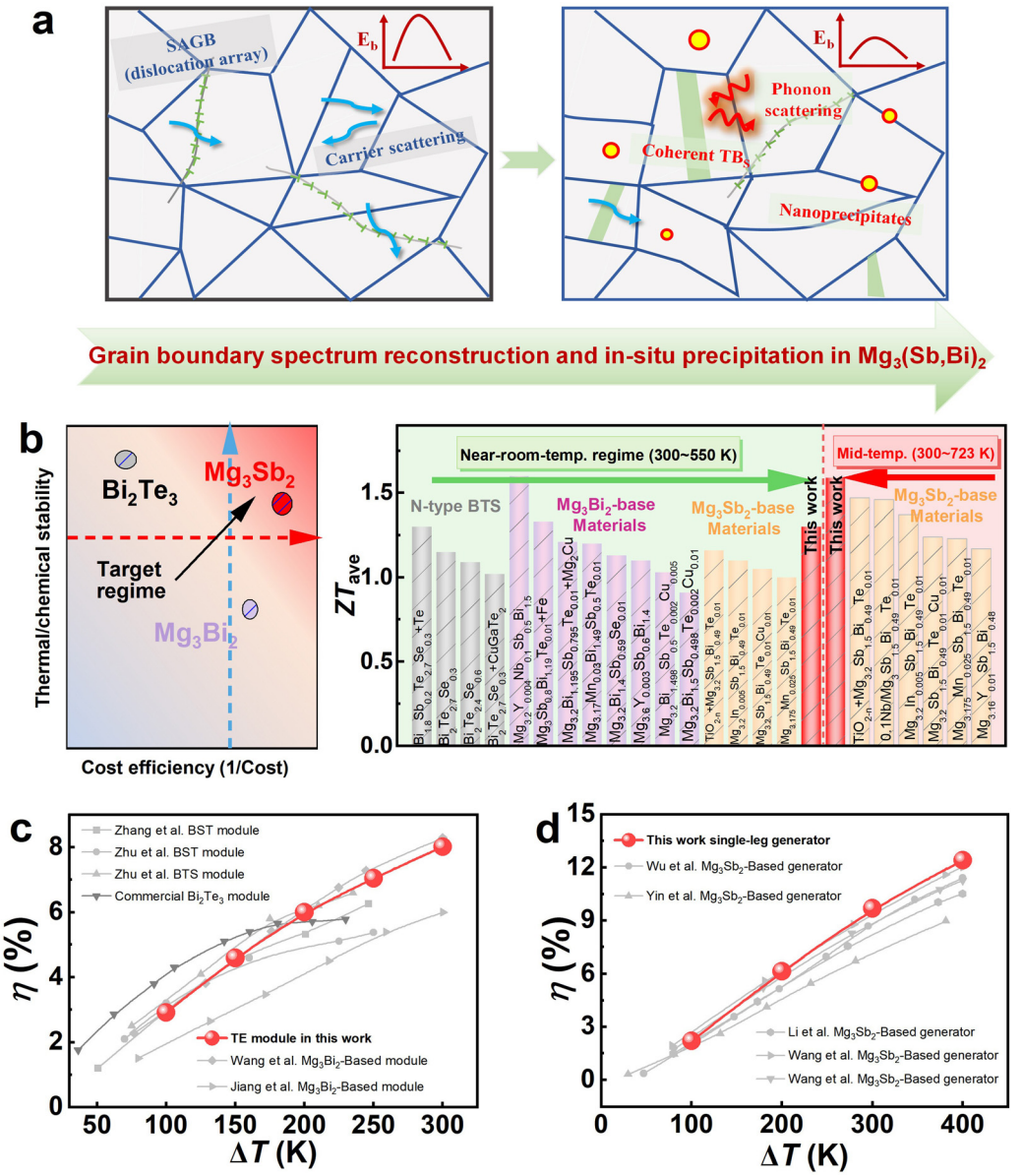

Fig. 1 The schematic of the main mechanism and superior thermoelectric performance in $Mg_3(Sb, Bi)_2$-based materials. (a) Schematic diagram of strain-mediated grain-boundary spectrum reconstruction and the dispersed *in situ* nanoprecipitates. (b) Raw-material cost and stability comparison, and the comparison of the average *ZT* values of this work with state-of-the-art n-type Bi_2Te_3-, Mg_3Bi_2-, and Mg_3Sb_2-based TE materials at different temperature ranges.[33,44–60] (c) The comparison of the conversion efficiency of the TE module in this work paired with a p-type MgAgSb material and previously reported Bi_2Te_3- and Mg_3Bi_2-based modules.[44,57,61–64] (d) The efficiency comparison between the single-leg generator and other Mg_3Sb_2-based systems.[57,60,65–68]

regime at the same time, as shown in Fig. 1b. In addition, a module paired with p-type MgAgSb delivers 8% conversion efficiency, exceeding that of the traditional Bi_2Te_3-based module, and a single TE-leg generator reaches 12.4% at $\Delta T = 400$ K, confirming its strong device-level competitiveness under the same temperature difference, as shown in Fig. 1c and d. This strategy establishes grain-boundary spectrum reconstruction as an effective lever to enable high near-room-temperature performance and bridge the performance-gap challenge in n-type Mg_3Sb_2 alloys, offering promising prospects for wide-ranging waste-heat recovery.

Results

Strain-mediated grain-boundary spectrum reconstruction optimizing near-room-temperature transport

Fig. S1a presents the powder XRD patterns of $Mg_{3.2(1-x)}Cu_xGa_xSb_{1.5(1-x)}Bi_{0.5(1-x)}Te_{2x}$ (x = 0, 0.003, 0.005, 0.007, and 0.009) samples at room temperature, where all the diffraction peaks are consistent with the Mg_3Sb_2-type phase (JCPDS# 03-0375), indicating a single-phase structure without detectable impurities within the sensitivity of XRD. The enlarged view of the (101) peaks reveal a slight shift toward lower diffraction angles at low

doping contents, followed by a reverse shift at higher doping levels. The refined lattice parameters in Fig. S1b and c show a similar trend. The initial lattice expansion results from the incorporation of atoms into interstitial positions,[58,69] whereas the subsequent contraction is attributed to the segregation of Cu–Ga-rich nanoprecipitates at higher doping levels, which will be discussed later.

Based on the XRD patterns given above, the effect of $CuGaTe_2$ additive incorporation on charge transport was further analyzed. GB scattering is a major limiting factor for the electrical transport of Mg_3Sb_2-based materials, particularly near room temperature. The thermoelectric performance of the pristine sample is shown in Fig. S2. With increasing temperature, it undergoes an N–P transition. As shown in Fig. 2a, with increasing doping content, the dominant carrier scattering mechanism gradually shifts from GB scattering toward acoustic phonon scattering, and the temperature-dependent exponent varies from $T^{-0.2}$ for the x = 0.003 to $T^{-0.78}$ for the x = 0.009 samples. Compared with the only Te-doped counterparts reported previously,[9,58] the samples after the additive incorporation exhibit a markedly weaker GB scattering. In addition, to further clarify the role of the additive, we also prepare a Te-only doped sample using the same preparation process, whose performance is presented in Fig. S3, and find pronounced GB scattering near room temperature. In addition, we plot $\ln(\sigma T^{1/2})$ as a function of $(1/k_BT)$ and fit the approximately linear near-room-temperature region to estimate the apparent E_b for each composition. As we can see from Fig. S4, the E_b of the pristine sample is 34 meV, which is similar to the reported value.[9,67] After $CuGaTe_2$ incorporation, the fitted E_b is markedly reduced compared with the Te-only doped sample, which quantitatively supports our original conclusion that the additive weakens the GB blocking effect. For the heavily added x = 0.009 sample, the fitted near-room-temperature region no longer shows a physically meaningful negative slope in the Seto plot. The nearly flat slope for x = 0.009 indicates that the simple activated-barrier description is no longer strictly applicable. While this does not weaken our conclusion, the quantitative analysis of the compositions is already sufficient to demonstrate that $CuGaTe_2$ incorporation substantially lowers the grain-boundary potential barrier. Generally, reduction of GB scattering in Mg_3Sb_2-based materials is obtained by grain coarsening. For instance, Liu *et al.* improved the performance of n-type $Mg_3Sb_{1.5}Bi_{0.5}$ by doping a small amount of Cu. That

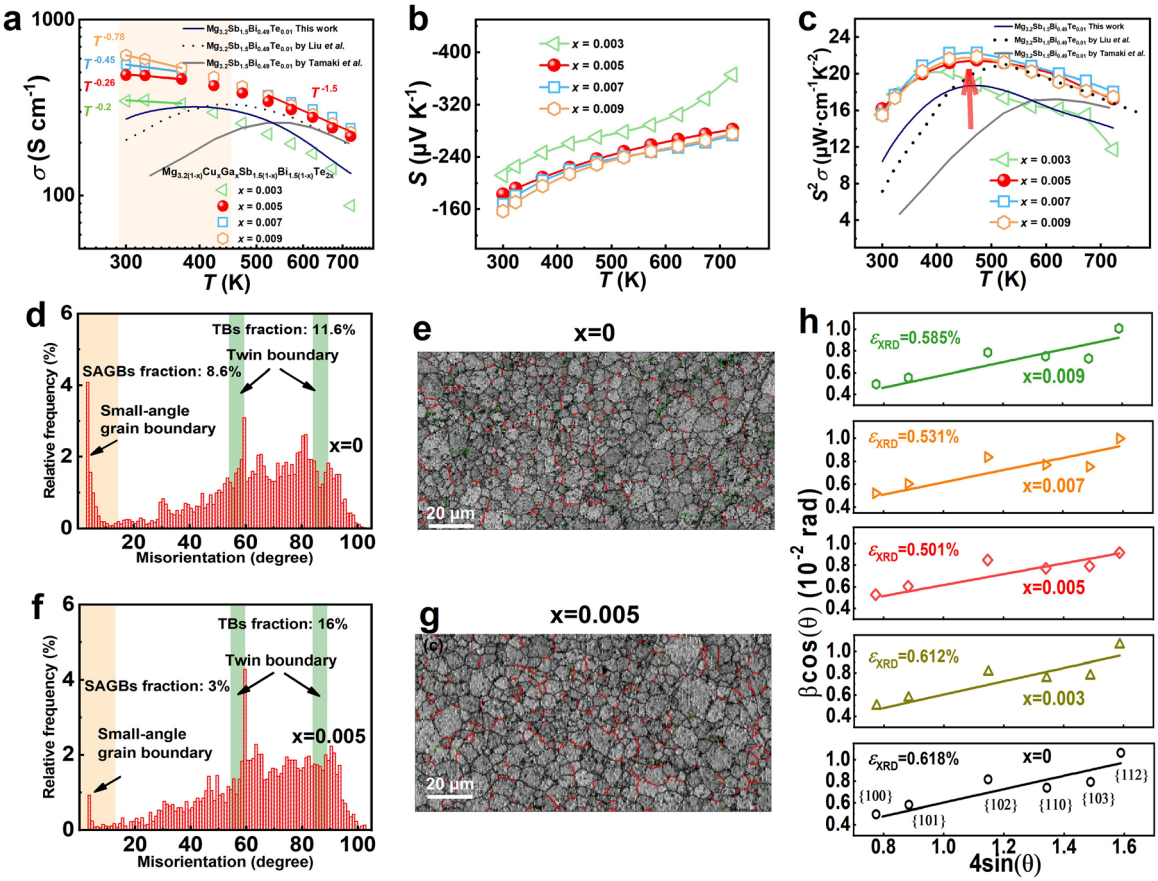

Fig. 2 The temperature-dependent electrical transport properties and microstructural evolution. The temperature-dependent electrical transport properties of $Mg_{3.2(1-x)}Cu_xGa_xSb_{1.5(1-x)}Bi_{0.5(1-x)}Te_{2x}$ samples: (a) electrical conductivity, (b) Seebeck coefficient, and (c) power factor. The grain misorientation distributions and corresponding morphology maps for (d and e) x = 0 and (f and g) x = 0.005 samples. TBs are marked in red and SAGBs are shown in green. (h) The internal strain analysis of samples.

work proposed two major effects of Cu addition: interstitial Cu in the lattice, which modifies the phonon structure and suppresses lattice thermal conductivity, and grain-boundary complexion engineering associated with Mg_2Cu eutectic wetting to enhance grain growth.[58] And Lei *et al.* deliberately introduced it as a nano-sintering aid at grain boundaries to promote grain growth. The average grain size increases up to 23.7 μm, which dramatically suppresses the grain-boundary scattering and improves the carrier mobility.[33] In contrast, the EBSD results in this work displayed in Fig. S5 reveal a little change in grain size after additive addition. Based on the statistical results summarized in Table S1 and Fig. S6, the mean grain sizes of the selected samples are 5.04, 5.60, and 5.20 μm, the median grain sizes are 4.54, 4.88 and 4.59 μm, and the standard deviations are 1.54, 1.57 and 1.47 μm for $x = 0$, $x = 0.005$ and $x = 0.009$, respectively. All these statistical parameters vary only within a small range, indicating that the grain-size distributions remain broadly comparable rather than showing substantial coarsening. Therefore, grain growth may make a limited contribution. Instead, compared with the relatively modest grain-size variation, the evolution in grain-boundary character is much more pronounced, which will be discussed later. According to Seto's grain boundary potential barrier model,[30] the observed behavior can be attributed to a reduction in the density of trapping states, which lowers the potential barrier height (E_b).

The Seebeck coefficients of the samples as a function of temperature are shown in Fig. 2b. All samples exhibit a negative Seebeck coefficient value and it increases monotonically with temperature, confirming n-type conduction behavior. With increasing additive content, the value of the Seebeck coefficient gradually decreases, primarily owing to the rise of carrier concentration (n), as shown in Fig. S7. According to the single parabolic band model,[70] the relationship between n and S is plotted in Fig. S8, revealing a moderate increase in the density of states effective mass. This trend may be related to a slight perturbation of the electronic structure induced by Ga incorporation. Similar behavior has been documented previously.[71] As a result, owing to effectively weakened GB scattering, the sample's power factor achieves a remarkable enhancement near room temperature (Fig. 2c), ensuring a more balanced performance across a broad temperature range.

To elucidate the origin of the reduced GB scattering, the structural evolution of samples is systematically examined. The results of the EBSD analysis are displayed in Fig. 2d–g and Fig. S9. In $Mg_3(Sb, Bi)_2$-based alloys, two representative twin modes form under different stress states, compression twins with a 56° misorientation and extension twins with a 86°, where the rotations are both at the $\langle 11\bar{2}0 \rangle$ axis. From the EBSD results, the grain boundary network undergoes significant reconstruction, accompanied by a marked increase in twin boundaries (TBs). Coherent TBs introduce far less lattice disorder than general grain boundaries, since their lattice mismatch is considerably smaller. TBs are closely correlated with strain relaxation. Williamson–Hall analysis based on XRD, as shown in Fig. 2h, provides a spatially averaged descriptor of diffraction-peak-broadening-related microstrain, and thus may approximately reflect the evolution of average lattice distortion. The calculation details are provided in the supplementary information (SI). The extracted ε_{XRD} is regarded as a spatially averaged parameter, especially in the present defect-rich system where dislocations, small-angle grain boundaries and precipitate-related interfaces may all contribute to peak broadening. Nevertheless, the overall trend of ε_{XRD} remains broadly consistent with the EBSD-observed grain-boundary spectrum evolution and defect-state changes. Specifically, the reduced ε_{XRD} in the optimized sample is interpreted as being consistent with a lower average lattice distortion, whereas the slight increase at higher additive content may be associated with the introduction of more incoherent interfaces due to precipitate coarsening. These results are considered together with the observed changes in twin-boundary fraction, KAM and dislocation density. The coarser precipitates, KAM and dislocation density will be discussed latter. Therefore, rather than relying on the Williamson–Hall analysis alone, the combined evidence is interpreted as being broadly consistent with strain-mediated grain-boundary spectrum reconstruction in this work.

Normally, the presence of small-angle grain boundaries (SAGBs) formed by dislocation clusters, along with semi-coherent interfaces and dopant-induced lattice distortions, could result in internal strain. Such accumulated strain energy may provide thermodynamic driving forces for strain-mediated microstructural reorganization, during which low-energy coherent twins preferentially form and partially replace high-energy grain boundaries, leading to a pronounced increase in the fraction of TBs and strain relaxation. In Fig. S10, we can also see a higher density of TBs in the $x = 0.005$ sample at the magnified misorientation analysis. In addition, the lower dislocation density and reduced Kernel Average Misorientation (KAM) values in the $x = 0.005$ sample, shown in Fig. S11 and S12, are consistent with the decreased proportion of SAGBs. Consequently, this strain-mediated grain-boundary spectrum reconstruction increases the fraction of coherent TBs while reducing high-angle grain boundaries with a high potential barrier height, thereby lowering the grain boundary scattering and optimizing the electrical transport near room temperature. To further illustrate the function of the additive $CuGaTe_2$, the Cu–Te control sample with a similar nominal additive level is prepared as shown in Fig. S13 and S14. In sharp contrast to the $CuGaTe_2$-doped samples, the Cu–Te control exhibits pronounced grain coarsening, whereas the twin boundary fraction remains essentially unchanged. Therefore, the weakened GB scattering is consistent with the grain-growth route. These comparisons indicate that Cu incorporation alone can indeed mitigate GB scattering *via* grain coarsening, but it does not reproduce the characteristic microstructural response observed with $CuGaTe_2$ addition. Therefore, the near-room-temperature transport improvement in the $CuGaTe_2$ case is consistent with strain-mediated grain-boundary spectrum reconstruction that promotes twin-boundary formation and reduces high-angle grain boundaries with a high potential barrier height.

Broad-scale *in situ* nanoprecipitates for phonon scattering and wide-range *ZT* enhancement

The temperature-dependent thermal transport behaviour is illustrated in Fig. 3. As shown in Fig. 3a, the κ_{tot} indicates a

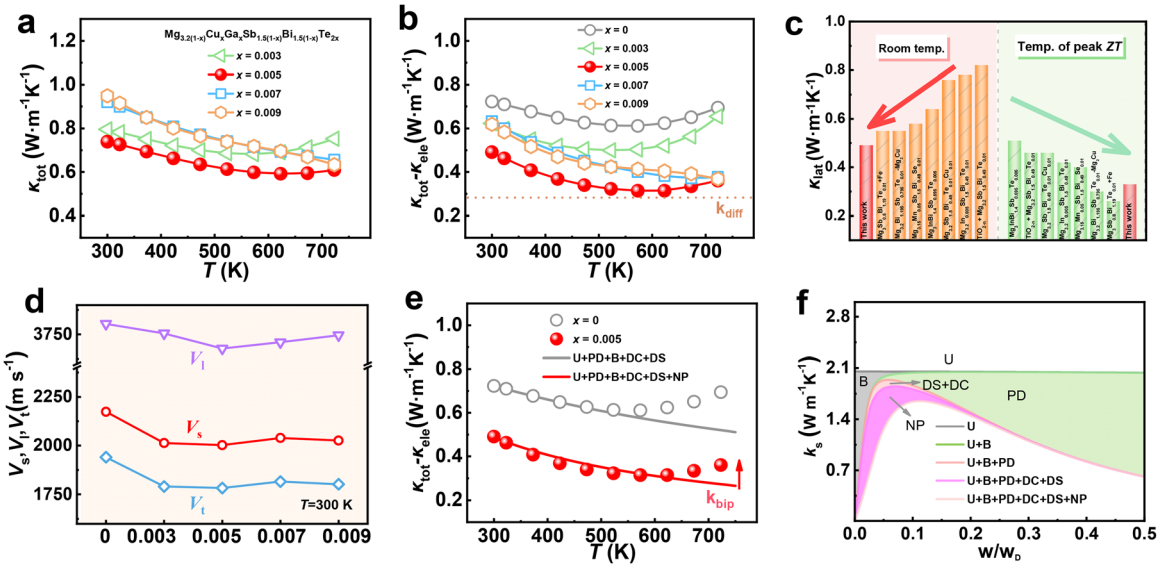

Fig. 3 The temperature-dependent thermal transport properties. (a) κ_{tot}, (b) κ_{tot}–κ_{ele}, (c) comparison of κ_{lat} between this work and previous reports, (d) sound velocities, (e) the combined contributions from κ_{bip} and κ_{lat}, and the (f) frequency-dependent κ_s of the x = 0.005 sample at room temperature, modelled using the Debye–Callaway approach.

nonmonotonic variation with additive content and exhibits that it initially decreases and then increases slightly at a higher doping content. This trend mainly reflects the evolution of electronic thermal conductivity (κ_{ele}), which is calculated using the Wiedemann–Franz law, $\kappa_{ele} = L\sigma T$, where the Lorenz number L is estimated through an empirical relationship.[72] Since the κ_{ele} is primarily determined by the σ, the contribution of the lattice component is obtained by κ_{tot}–κ_{ele}, as shown in Fig. 3b. The κ_{tot}–κ_{ele} values experience a temperature dependence, initially decreasing and then rising at elevated temperatures, mainly due to the activation of the bipolar effect. Obviously, the bipolar effect is progressively suppressed with increasing additive content because of the higher carrier concentration inhibiting minority carrier excitation, consistent with Fig. S7. The lowest κ_{lat} reaches 0.31 W m^{-1} K^{-1} for the x = 0.005 at 573 K, approaching the theoretical minimum predicted by the phonon diffusion limit. The calculation details of the theoretical minimum can be seen in the SI. Compared with the pristine sample, all doped samples display a substantially reduced κ_{lat}, which can be attributed to Cu-induced modification. It can introduce additional phonon channels and weaken the acoustic stiffness of Mg_3Sb_2.[58] This can be supported by the reduced sound velocity in Fig. 3d and the red shift of Raman peaks in Fig. S15. However, the negligible difference in sound velocity among doped samples suggests that the further variation of κ_{lat} originates from some other factors rather than intrinsic lattice softening. In addition, the obtained κ_{lat} in this work, shown in Fig. 3c, is lower than most reported n-type Mg_3Sb_2-based materials both at room temperature and extremely near the ZT_{max} regime, assuring a balanced performance at a wide temperature range.[33,49,55,57,58,73,74]

To further elucidate the phonon transport behavior and microstructural evolution, STEM characterization is performed. From the low-magnification images shown in Fig. 4a–c, these reveal numerous dislocations and uniformly dispersed nanoprecipitates across the matrix, consistent with the multi-region observations in Fig. S16. Dislocations represent atomic misalignments and act as two-dimensional line defects capable of effectively scattering mid-frequency phonons. Meanwhile, the nanoprecipitates exhibit a broad size distribution ranging from several nanometers to hundreds of nanometers, contributing to broad scale phonon scattering. Specifically, nanoprecipitates with sizes of a few to tens of nanometers can effectively scatter high-frequency phonons, which have a strong phonon scattering ability, and larger submicron precipitates with weaker scattering strength that mainly interact with low-frequency phonons, jointly leading to suppressed κ_{lat}. In addition, the elemental mappings in Fig. 4d and e demonstrate uniform distributions of Mg, Sb, Bi and Te, while Cu and Ga exhibit localized enrichment, confirming the formation of Cu–Ga-rich nanoprecipitates. According to the isothermal Cu–Ga–Te ternary phase diagram and the Cu–Ga binary phase diagram shown in Fig. S17 and S18, $CuGaTe_2$ is not expected to remain chemically unchanged under Te-deficient processing conditions. Instead, after partial dissolution and local redistribution during milling or sintering, the local composition can shift toward the Cu–Ga side, making subsequent phase partitioning into Cu–Ga-rich precipitates. As shown in Fig. 4f and Fig. S16 of the high-resolution TEM images, these nanoprecipitates are located within grains or along grain boundaries, and some of the precipitates maintain coherent or semi-coherent interfaces with the matrix. These partially incoherent interfaces could generate the localized lattice strain, as evidenced by the geometric phase analysis (GPA) strain maps (Fig. 4g). The corresponding Inverse Fast Fourier Transform (IFFT) image in Fig. 4h indicates some dislocations surrounding these nanoprecipitates, consistent

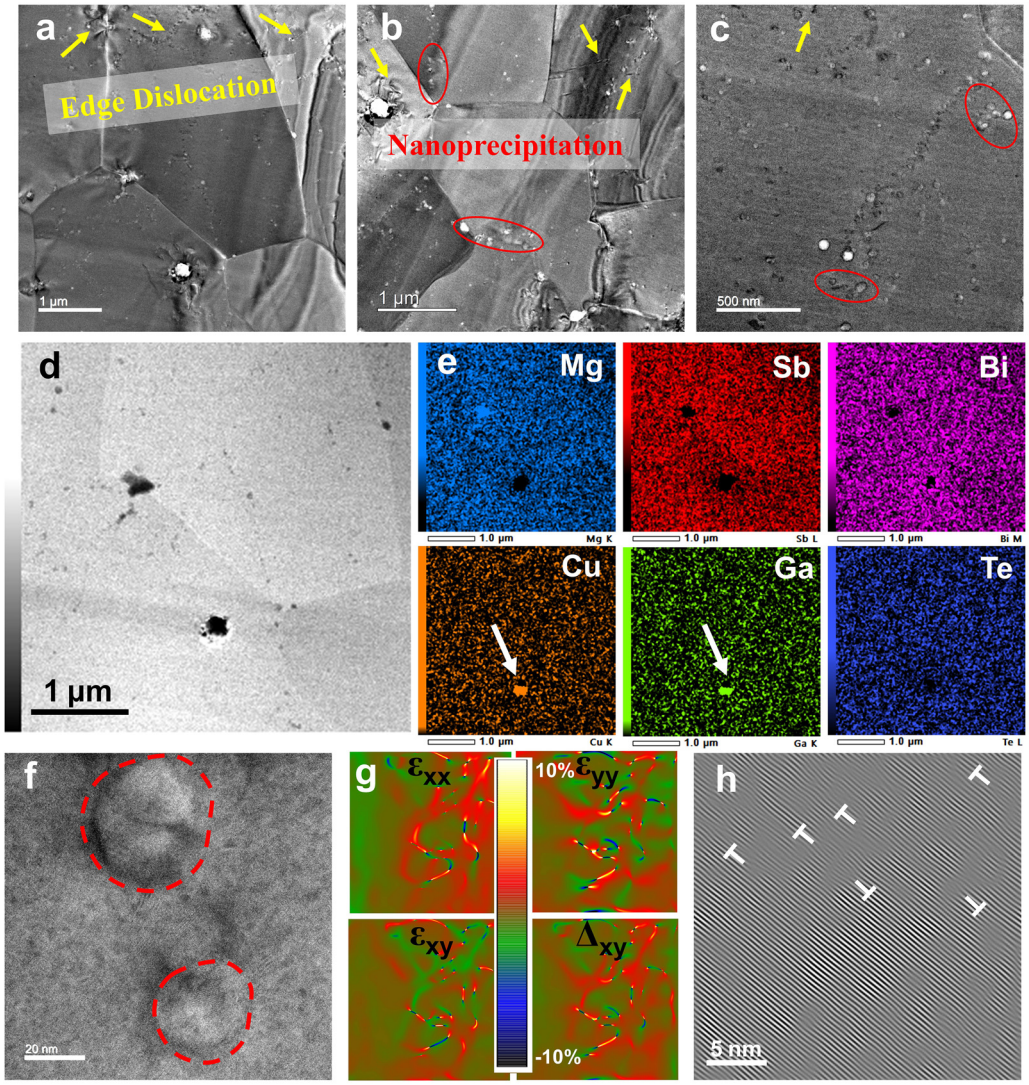

Fig. 4 STEM microstructural analysis of the x = 0.005 sample. (a–c) The STEM images showing a high density of lattice defects, with yellow arrows denoting dislocations and red circles highlighting nanoprecipitations. (d and e) EDS elemental distribution maps of Mg, Bi, Sb, Cu, Ga and Te. (f) High-resolution STEM image of nanoprecipitations and (g) corresponding strain maps derived from geometric phase analysis (GPA) and (h) the inverse FFT (IFFT) image illustrating dislocation distributions.

with the strain distortion. The presence of such broad scale defects, particularly those in the nanometer range of precipitates, serves as efficient phonon-scattering centers, thereby contributing to the substantial reduction of κ_{lat}.

As shown in Fig. S19 and S20, the EPMA is adopted to verify the spatial distribution and composition of precipitates in a wide area on the x = 0.005 and x = 0.009 samples. Both samples exhibit homogeneous distributions of Mg, Sb, Bi and Te elements, while Cu and Ga show clear localized enrichment, consistent with the STEM observations. Clearly, the Cu–Ga-rich precipitates in the x = 0.005 sample are extremely fine whereas those in the x = 0.009 sample coarsen significantly to the micrometer scale, which can be attributed to the growth of Cu–Ga intermetallics on further additive addition. Based on the isothermal Cu–Ga–Te ternary phase diagram, the equilibrium composition of $CuGaTe_2$ is expected to shift toward the Cu–Ga side under Te-deficient conditions, making the formation of Cu–Ga-rich intermetallic precipitates thermodynamically plausible. Consistently, STEM/EPMA elemental mapping reveals localized enrichment of Cu and Ga, while Mg, Sb, Bi and Te remain comparatively homogeneous in the matrix. Moreover, EPMA point analyses in Tables S2 and S3 show very low Te contents in the precipitate-enriched regions, indicating that these precipitates are not Te-rich phases. According to the local Cu/Ga ratios together with the Cu–Ga phase diagram, these precipitates are therefore interpreted as Cu–Ga-rich phases, likely corresponding to Cu–Ga intermetallics.

As confirmed by STEM and EPMA analyses, the broad scale defects, particularly the nanometer range of precipitates, act as effective phonon-scattering centers. And these could suppress heat transport over a wide phonon spectrum. At higher doping levels, the coarsening of microscale Cu–Ga-rich precipitates

may weaken phonon scattering efficiency, leading to a modest increase in κ_{lat} as shown in Fig. 3b, whereas it remains low especially at high temperatures.

To further quantify the origin of the decreased κ_{lat}, the Debye–Callaway model is employed for theoretical analysis:[75]

$$\kappa_{lat} = \frac{k_B}{2\pi^2 \nu}\left(\frac{k_B T}{\hbar}\right)\int_0^{\theta_D/T} \tau_{tot}(x)\frac{x^4 e^x}{(e^x-1)^2}dx \qquad (3)$$

where $x = \hbar\omega/k_B T$, k_B, $\hbar$ and τ_{tot} denote the Boltzmann constant, reduced Planck constant, and total phonon relaxation time, respectively. Details are provided in Table S4. In this model, it considers multiple scattering processes, including phonon–phonon Umklapp (U), grain-boundary (B), point-defect (PD), dislocation (DC), strain-induced (DS) and nanoprecipitate (NP) scattering. The sound velocity used in the model corresponds to the experimentally measured values for each sample. As shown in Fig. 3e, the simulated κ_{lat} exhibits good agreement with the experimental data, validating that the reduced sound velocity and presence of nanoprecipitates dominate the suppression of κ_{lat} in doped samples. As we can see, the κ_{bip} is also notably mitigated due to enhanced carrier concentration. To gain further insight, the frequency-dependent κ_s for the $x = 0.005$ sample at room temperature is plotted in Fig. 3f. As we can see, the low-frequency phonons are mainly scattered by grain boundaries, while the intermediate-frequency phonons are additionally scattered by dislocations and strain fields. In the higher-frequency regime, point defects become particularly effective because their scattering rate increases strongly with phonon frequency. The precipitates with different sizes scatter phonons over different frequency ranges: the larger precipitates mainly scatter lower-frequency phonons, whereas the finer nanoscale precipitates are more effective for higher-frequency phonons. The analysis reveals that nanoprecipitates and point scattering contributes significantly to the reduction of κ_{lat}, consistent with the previous analysis of microstructural evolution. Thus, the broad scale defect network, especially the nanoscale precipitates, leads to phonon scattering over broad frequency ranges and substantially depresses κ_{lat}.

As a result, by integrating strain-mediated grain-boundary spectrum reconstruction with the formation of broad-scale *in situ* Cu–Ga-rich nanoprecipitates, the additive-enabled effect establishes a synergistic optimization between electron and phonon transport. As shown in Fig. 5a, the ratio of weighted mobility (μ_w) to κ_{lat} provides a comprehensive indicator of the electron and phonon balance in this work. The calculation method for weighted mobility is displayed in the SI. The values increase markedly after additive incorporation and reach a maximum at $x = 0.005$, consistent with the previous analysis. Furthermore, a maximum ZT of 2.08 at 623 K is achieved, while high ZT values persist throughout the measured temperature

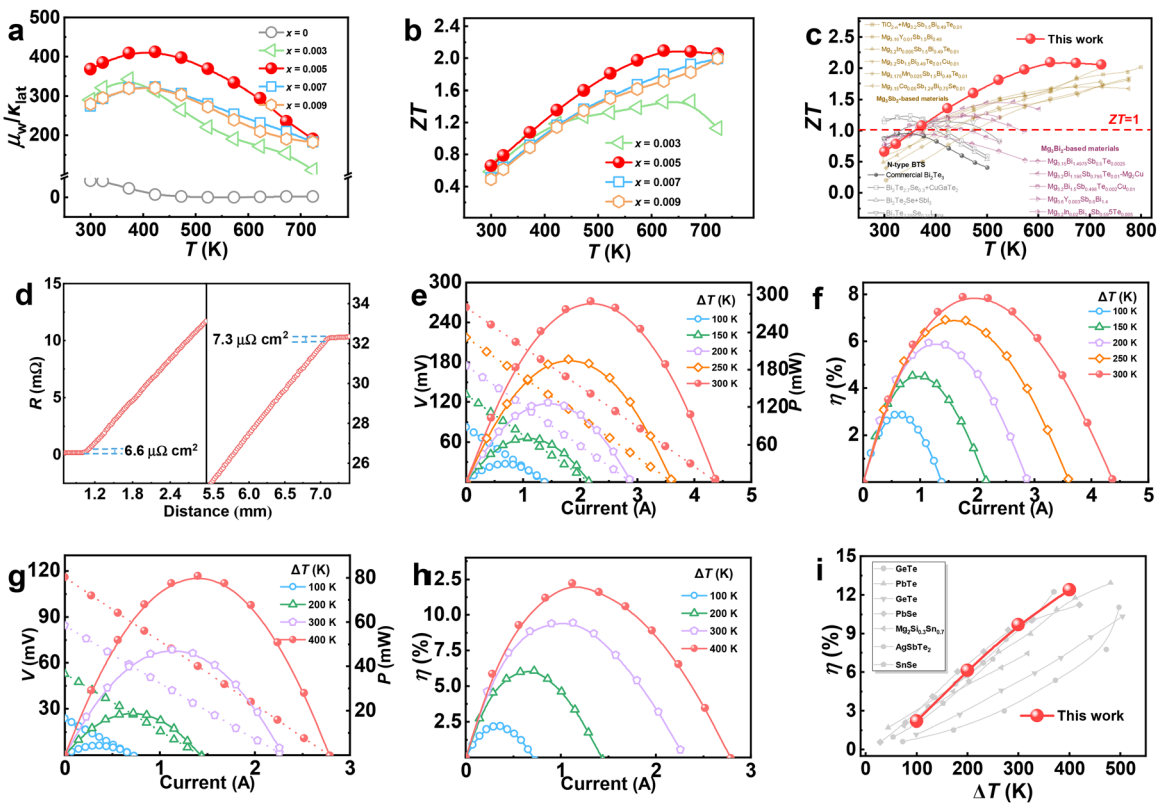

Fig. 5 The thermoelectric performance: ZT values, the fabricated single-leg device and TE module. (a) μ_w/κ_{lat}, (b) ZT, (c) comparison of ZT values with representative n-type thermoelectric systems, including Bi_2Te_3-, Mg_3Bi_2- and Mg_3Sb_2-based materials, (d) the measured contact resistance, (e and f) I–V and I–P characteristics and conversion efficiency (η) of the TE module under different temperature differences, (g and h) I–V and I–P curves and η of the single-leg generator at various temperature gradients, and (i) comparison of the conversion efficiency between this work and reported single-leg devices.

range plotted in Fig. 5b. Although the x = 0.009 sample still retains some beneficial structural evolution for charge transport, the deterioration in thermal transport becomes more significant owing to the coarser precipitates. So, the negative effect on thermal properties outweighs the gain in electrical properties, leading to a slightly lower overall thermoelectric performance than that of the x = 0.005 sample. Remarkably, the near-room-temperature ZT surpasses that of commercial n-type Bi_2Te_3-based materials and rivals that of the Mg_3Bi_2-rich counterparts that dominate the room-temperature regime, as displayed in Fig. 5c.[33,47,52,54,55,57–60,74,76–80] This achievement effectively bridges the long-standing performance gap between Mg_3Sb_2-rich mid-temperature materials and Mg_3Bi_2-rich near-room-temperature systems, realizing a broad-range high TE performance window from room temperature to above 700 K. To verify reproducibility, multiple samples of x = 0.005 were prepared and tested, showing highly consistent TE properties, as plotted in Fig. S21.

These strategies, including strain-mediated grain-boundary spectrum reconstruction and broad scale *in situ* Cu–Ga-rich nanoprecipitates, orchestrate broad-range thermoelectric performance and highlight the effectiveness. To further validate the practical potential of the optimized $Mg_{3.2(1-x)}Cu_xGa_xSb_{1.5(1-x)}Bi_{0.5(1-x)}Te_{2x}$ materials, a TE module and single-leg device are fabricated. Primarily, the finite element numerical simulation is carried out to refine the device architectures and determine the most efficient structural configuration. The refined geometries are plotted in Fig. S22 and S23. As shown in Fig. 5d, the contact resistance between the TE materials and barrier layer is remarkably low, suggesting good electrical coupling at the interface. In addition, the interfacial structure, as indicated by the SEM image and its elemental mapping shown in Fig. S24, reveals a continuous interface without detectable pores or elemental diffusion. The well bonded and chemically stable interfaces ensure the thermal and mechanical reliability of TE device. The TE conversion behaviour of fabricated devices is also systematically evaluated. Fig. 5e–h display the I–V and I–P characteristics and conversion efficiency (η) of the TE module and single-leg generator under different temperature differences. As we can see, the open-circuit voltage (V) of the TE module increases progressively with the applied temperature difference, consistent with the Seebeck effect. The corresponding I–P curves exhibit the typical parabolic dependence, and it reaches its maximum value when the external resistance is the same as the internal resistance. The internal resistance determined from the slope of the I–V curve increases slightly with temperature due to the decrease in electrical conductivity, as shown in Fig. S25 and S26. Meanwhile, as the current increases, the output heat flow also rises, reflecting the combined contribution of Joule and Peltier effects. Thus, a module paired with p-type MgAgSb achieves a conversion efficiency of 8% at ΔT = 300 K, surpassing that of conventional Bi_2Te_3-based modules in the near-room-temperature range. For reproducibility, we remeasured the fabricated two-pair module, as displayed in Fig. S27, and there is good reproducibility in their efficiency performance under the same test conditions. In addition, a single-leg generator attains η = 12.4% at ΔT = 400 K. As illustrated in Fig. 5i,[81–85] the comparison of single-leg efficiencies across various TE systems highlights the superior performance of our device at the same testing temperature, confirming its feasibility for practical power generation. These device-level achievements convincingly demonstrate the effectiveness of the strain-mediated grain-boundary spectrum reconstruction and *in situ* nanoprecipitate strategy, which successfully bridges the long-standing performance gap between near-room and mid-temperature TE regimes, enabling efficient power generation across a broad temperature window.

Discussion

In summary, this work demonstrates that strain-mediated grain-boundary spectrum reconstruction and broad scale *in situ* nanoprecipitates can serve as an effective route to reconcile near-room-temperature and mid-temperature thermoelectric performance in n-type Mg_3Sb_2. By utilizing $CuGaTe_2$ as a multifunctional additive, subtle lattice perturbations drive a reconfiguration of the grain boundary spectrum, markedly increasing the fraction of coherent twin boundaries and reducing grain-boundary potential barriers. This grain boundary spectrum engineering restores the power factor especially the near-room-temperature regime. Notably, the processing-induced compositional fluctuations give rise to *in situ* nanoscale phase partitioning forming multi-length-scale phonon-scattering architectures that suppress lattice thermal conductivity to 0.49 W m^{-1} K^{-1} without degrading electronic transport. As a result, the Mg_3Sb_2 system yields an impressive average ZT of 1.3 at ΔT = 250 K, surpassing that of most reported n-type Bi_2Te_3-based materials near room temperature, and maintains a high average ZT of 1.59 (300–723 K), exhibiting superiority in the mid-temperature regime as well. Moreover, the assembled devices deliver outstanding conversion efficiencies of 8% at ΔT = 300 K and 12.4% at ΔT = 400 K, confirming strong device-level competitiveness. These findings suggest a potentially useful route to achieve high thermoelectric performance from a near-room to mid-temperature window for waste-heat recovery applications.

Methods

Sample synthesis

Polycrystalline samples with nominal compositions of $Mg_{3.2(1-x)}Cu_xGa_xSb_{1.5(1-x)}Bi_{0.5(1-x)}Te_{2x}$ (x = 0, 0.003, 0.005, 0.007, and 0.009) were synthesized from high-purity Mg (4N), Sb (4N), Bi (4N) and $CuGaTe_2$ powders, where Cu, Ga and Te were introduced in the form of the ternary additive $CuGaTe_2$. The mixed raw materials were placed in a ball mill and milled for 5 h (SPEX-Sample Prep 8000 Mixer Mill). The milled powders were loaded into a graphite die (∅ 10 mm) in an argon atmosphere and densified by SPS (SPS-1080 System, SPS SYNTEX INC) at 973 K under 60 MPa for 20 minutes. The p-type MgAgSb material was synthesized with a nominal composition of $MgAg_{0.97}Sb_{0.99}$ (referred to as MgAgSb) using Mg turnings, Ag powder, Sb shots and 0.75 wt% $C_{18}H_{36}O_2$. All raw materials were weighed based

on the target stoichiometry and sealed in a ball-milling jar under an argon atmosphere. The mixture was mechanically alloyed for 5 h, followed by vacuum spark plasma sintering at 573 K and 60 MPa for 5 min to obtain the bulk sample. The $CuGaTe_2$ powders were self-synthesized by sealing stoichiometric amounts of high-purity Cu (4N), Ga (4N) and Te (4N) in an evacuated quartz tube, followed by heating to 1373 K at a rate of 30 K min^{-1}, holding for 10 hours, and then furnace-cooling to room temperature. The phase purity of the obtained $CuGaTe_2$ was confirmed by XRD, as shown in Fig. S28.

Measurement and characterization

The commercial instrument ZEM-3 (ULVAC ZEM-3) was used to test the σ and$S$ of the samples in a helium atmosphere. The κ_{tot} was derived from $\kappa_{tot} = D\rho C_p$. Here, D was measured using a Netzsch LFA 467 instrument, ρ was obtained based on the Archimedes principle, and C_p was evaluated using the formula $C_p = 3NR\,(1 + 1.3 \times 10^{-4}\,T - 4 \times 10^{3}\,T^{-2})/M$.[86] Room-temperature carrier concentration (n) and carrier mobility (μ) were obtained from Hall-effect measurements performed on a PPMS (Physical Properties Measurement System, Quantum Design).

The structural and microstructural characterization of the sample was performed by X-ray diffraction (SmartLab3, Rigaku), Electron Backscatter Diffraction (EBSD, JSM-7001F, JEOL Inc.), Scanning Electron Microscopy (SEM, Hitachi SU4800), Electron Probe Microanalysis (EPMA, JXA-8500F), Raman spectroscopy (inVia, Renishaw) and Scanning Transmission Electron Microscopy (STEM, JEM-ARM-200F-B). The sound velocity at 300 K was measured using an ultrasonic system (UVM-2, Ultrasonic Engineering Co., Ltd).

Unless otherwise stated, the electrical conductivity, Seebeck coefficient, Hall properties and thermal transport properties shown for each composition were obtained from one independently prepared bulk sample. For the optimized composition x = 0.005, multiple independently prepared samples were further characterized in order to verify reproducibility.

TE module fabrication

A single-leg generator was fabricated using the ball-milled $Mg_{3.184}Cu_{0.005}Ga_{0.005}Sb_{1.4925}Bi_{0.4975}Te_{0.01}$ powder, sandwiched between Ni foils and 304 stainless-steel foils in a Ni/304 stainless-steel/sample powder/304 stainless-steel/Ni structure, followed by a one-step sintering process. The obtained ingot was cut into cuboids with dimensions of 3.4 × 3.4 × 6 mm^3. The two-pair thermoelectric module was assembled using n-type $Mg_{3.184}Cu_{0.005}Ga_{0.005}Sb_{1.4925}Bi_{0.4975}Te_{0.01}$ legs with dimensions of 3.5 × 3.5 × 6 mm^3 and p-type MgAgSb legs. The conversion efficiency was measured using a Mini-PEM (Advance Riko, Japan). The properties of p-type MgAgSb are shown in Fig. S29. Further descriptions of the simulation procedures can be found in the SI.

Author contributions

G. W.: conceptualization, methodology, investigation, formal analysis, data curation, and writing–original draft. A. L.: writing–review and editing. H. S. I.: discussion and writing–review and editing. L. W.: discussion and writing–review and editing. X. W.: discussion and writing–review and editing. J. L.: discussion and writing–review and editing. F. Y.: discussion and writing–review and editing. T. M.: conceptualization, supervision, and writing–review and editing.

Conflicts of interest

T. M. and G. W. have filed one Japanese patent application (2025-244532). The remaining authors declare no competing interests.

Data availability

All data generated or analysed during this study are included in this article (and its supplementary information, SI). The supplementary information contains additional experimental details, characterization data, thermoelectric and device measurement data, modelling details, and supporting figures and tables. See DOI: https://doi.org/10.1039/d6ee01515h.

Acknowledgements

This work was supported by the JST Mirai Program (JPMJMI19A1, T. M.).

References

1 L. E. Bell, *Science*, 2008, **321**, 1457–1461.
2 I. Petsagkourakis, K. Tybrandt, X. Crispin, I. Ohkubo, N. Satoh and T. Mori, *Sci. Technol. Adv. Mater.*, 2018, **19**, 836–862.
3 Q. Yan and M. G. Kanatzidis, *Nat. Mater.*, 2022, **21**, 503–513.
4 X. L. Shi, J. Zou and Z. G. Chen, *Chem. Rev.*, 2020, **120**, 7399–7515.
5 X. L. Shi, N. H. Li, M. Li and Z. G. Chen, *Chem. Rev.*, 2025, **125**, 7525–7724.
6 S. Bano, R. Chetty, J. Babu and T. Mori, *Device*, 2024, **2**, 100408.
7 T. Hendricks, T. Caillat and T. Mori, *Energies*, 2022, **15**, 2022.
8 G. J. Snyder and E. S. Toberer, *Nat. Mater.*, 2008, **7**, 105–114.
9 H. Tamaki, H. K. Sato and T. Kanno, *Adv. Mater.*, 2016, **28**, 10182–10187.
10 A. Li, C. Fu, X. Zhao and T. Zhu, *Research*, 2020, **2020**, 1934848.
11 H. Shang, Z. Liang, C. Xu, J. Mao, H. Gu, F. Ding and Z. Ren, *Research*, 2020, **2020**, 1219461.
12 W. Xu, B. A. Al-Maythalony, J. Li, X. Li, L. Fu and B. Xu, *Adv. Funct. Mater.*, 2024, **35**, 2414194.
13 P. Zhao, W. Xue, Y. Zhang, S. Zhi, X. Ma, J. Qiu, T. Zhang, S. Ye, H. Mu, J. Cheng, X. Wang, S. Hou, L. Zhao, G. Xie, F. Cao, X. Liu, J. Mao, Y. Fu, Y. Wang and Q. Zhang, *Nature*, 2024, **631**, 777–782.

14 H. Yang, P. Xu, B. A. Al-Maythalony, Y. Huang, M. Xu, Y. Hua, W. Zhang, X. Wang, S. Cui, H. Zhu and B. Xu, *Sci. Adv.*, 2026, **12**, eaed3783.
15 L. Wang, A. Li, X. Wu, J. Li, T. Ohsawa and T. Mori, *Adv. Mater.*, 2025, **37**, e2508270.
16 X. Shi, X. Wang, W. Li and Y. Pei, *Small Methods*, 2018, **2**, 1800022.
17 S. Ohno, K. Imasato, S. Anand, H. Tamaki, S. D. Kang, P. Gorai, H. K. Sato, E. S. Toberer, T. Kanno and G. J. Snyder, *Joule*, 2018, **2**, 141–154.
18 X. Wu, X. Ma, H. Yao, K. Liang, P. Zhao, S. Hou, L. Yin, H. Yang, J. Sui, X. Lin, F. Cao, Q. Zhang and J. Mao, *ACS Appl. Mater. Interfaces*, 2023, **15**, 50216–50224.
19 J. Zhang, L. Song, S. H. Pedersen, H. Yin, L. T. Hung and B. B. Iversen, *Nat. Commun.*, 2017, **8**, 13901.
20 A. Li, P. Nan, Y. Wang, Z. Gao, S. Zhang, Z. Han, X. Zhao, B. Ge, C. Fu and T. Zhu, *Acta Mater.*, 2022, **239**, 118301.
21 Q.-Q. Wang, K.-F. Liu, Y.-Y. Su, X.-C. Liu, Q. Liu, S. Zhou, J. Liu and S.-Q. Xia, *Acta Mater.*, 2023, **255**, 119028.
22 S. Xie, X. Wan, Y. Wu, C. Li, F. Yan, Y. Ouyang, H. Ge, X. Li, Y. Liu, R. Wang, M. Y. Toriyama, G. J. Snyder, J. Yang, Q. Zhang, W. Liu and X. Tang, *Adv. Mater.*, 2024, **36**, e2400845.
23 J. Mao, J. Shuai, S. Song, Y. Wu, R. Dally, J. Zhou, Z. Liu, J. Sun, Q. Zhang, C. Dela Cruz, S. Wilson, Y. Pei, D. J. Singh, G. Chen, C. W. Chu and Z. Ren, *Proc. Natl. Acad. Sci. U. S. A.*, 2017, **114**, 10548–10553.
24 W. Peng, G. Petretto, G.-M. Rignanese, G. Hautier and A. Zevalkink, *Joule*, 2018, **2**, 1879–1893.
25 R. Chetty, J. Babu and T. Mori, *Joule*, 2024, **8**, 556–562.
26 T. Mori, *Small*, 2017, **13**, 1702013.
27 J. J. Kuo, S. D. Kang, K. Imasato, H. Tamaki, S. Ohno, T. Kanno and G. J. Snyder, *Energy Environ. Sci.*, 2018, **11**, 429–434.
28 J. J. Kuo, Y. Yu, S. D. Kang, O. Cojocaru-Mirédin, M. Wuttig and G. J. Snyder, *Adv. Mater. Interfaces*, 2019, **6**, 1900429.
29 J. Mao, Y. Wu, S. Song, Q. Zhu, J. Shuai, Z. Liu, Y. Pei and Z. Ren, *ACS Energy Lett.*, 2017, **2**, 2245–2250.
30 J. Y. W. Seto, *J. Appl. Phys.*, 1975, **46**, 5247–5254.
31 M. Wood, J. J. Kuo, K. Imasato and G. J. Snyder, *Adv. Mater.*, 2019, **31**, e1902337.
32 K. Imasato, C. Fu, Y. Pan, M. Wood, J. J. Kuo, C. Felser and G. J. Snyder, *Adv. Mater.*, 2020, **32**, e1908218.
33 J. Lei, K. Zhao, J. Liao, S. Yang, Z. Zhang, T. R. Wei, P. Qiu, M. Zhu, L. Chen and X. Shi, *Nat. Commun.*, 2024, **15**, 6588.
34 T. Luo, J. J. Kuo, K. J. Griffith, K. Imasato, O. Cojocaru-Mirédin, M. Wuttig, B. Gault, Y. Yu and G. J. Snyder, *Adv. Funct. Mater.*, 2021, **31**, 2100258.
35 C. Hu, K. Xia, C. Fu, X. Zhao and T. Zhu, *Energy Environ. Sci.*, 2022, **15**, 1406–1422.
36 R. Wu, Y. Yu, S. Jia, C. Zhou, O. Cojocaru-Miredin and M. Wuttig, *Nat. Commun.*, 2023, **14**, 719.
37 Y. Yu and M. Wuttig, *Nano Res. Energy*, 2023, **2**, e9120057.
38 G. Li, J. He, Q. An, S. I. Morozov, S. Hao, P. Zhai, Q. Zhang, W. A. Goddard and G. J. Snyder, *Acta Mater.*, 2019, **169**, 9–14.
39 H. Wang, S. Zheng, H. Wu, X. Xiong, Q. Xiong, H. Wang, Y. Wang, B. Zhang, X. Lu, G. Han, G. Wang and X. Zhou, *Small*, 2022, **18**, e2104592.
40 A. Zhang, B. Zhang, W. Lu, D. Xie, H. Ou, X. Han, J. Dai, X. Lu, G. Han, G. Wang and X. Zhou, *Adv. Funct. Mater.*, 2018, **28**, 1705117.
41 G. Tan, F. Shi, S. Hao, L. D. Zhao, H. Chi, X. Zhang, C. Uher, C. Wolverton, V. P. Dravid and M. G. Kanatzidis, *Nat. Commun.*, 2016, **7**, 12167.
42 K. Biswas, J. He, I. D. Blum, C. I. Wu, T. P. Hogan, D. N. Seidman, V. P. Dravid and M. G. Kanatzidis, *Nature*, 2012, **489**, 414–418.
43 K. Biswas, J. He, Q. Zhang, G. Wang, C. Uher, V. P. Dravid and M. G. Kanatzidis, *Nat. Chem.*, 2011, **3**, 160–166.
44 B. Zhu, X. Liu, Q. Wang, Y. Qiu, Z. Shu, Z. Guo, Y. Tong, J. Cui, M. Gu and J. He, *Energy Environ. Sci.*, 2020, **13**, 2106–2114.
45 Y. Liu, Y. Zhang, K. H. Lim, M. Ibanez, S. Ortega, M. Li, J. David, S. Marti-Sanchez, K. M. Ng, J. Arbiol, M. V. Kovalenko, D. Cadavid and A. Cabot, *ACS Nano*, 2018, **12**, 7174–7184.
46 B. Zhu, Z.-Y. Huang, X.-Y. Wang, Y. Yu, L. Yang, N. Gao, Z.-G. Chen and F.-Q. Zu, *Nano Energy*, 2017, **42**, 8–16.
47 G. Wu, Q. Zhang, X. Tan, Y. Fu, Z. Guo, Z. Zhang, Q. Sun, Y. Liu, H. Shi, J. Li, J. G. Noudem, J. Wu, G. Q. Liu, P. Sun, H. Hu and J. Jiang, *Adv. Mater.*, 2024, **36**, e2400285.
48 H. Yang, B. Jia, L. Xie, D. Mao, J. Xia, J. Yang, M. Yuan, Q. Gan, X. Liu, M. Hu, J. Shuai and J. He, *Joule*, 2024, **8**, 2667–2680.
49 K. Jin, H. Nie, F. Gao, J. J. Ma, M. Shu, X. Yan, Z. H. Ge, X. Gao, W. Zhao, M. Liu, Y. Yu, J. Ma, B. Xu and L. Fu, *Adv. Funct. Mater.*, 2024, **35**, 2418041.
50 K. Yang, X. Li, C. Sun, W. Song, W. Zhao and Q. Zhang, *Adv. Funct. Mater.*, 2024, **34**, 2315886.
51 X. Mo, J. Liao, G. Yuan, S. Zhu, X. Lei, L. Huang, Q. Zhang, C. Wang and Z. Ren, *J. Magnesium Alloys*, 2022, **10**, 1024–1032.
52 P. Ying, L. Wilkens, H. Reith, N. P. Rodriguez, X. Hong, Q. Lu, C. Hess, K. Nielsch and R. He, *Energy Environ. Sci.*, 2022, **15**, 2557–2566.
53 H. Cho, S. Y. Back, N. Sato, Z. Liu, W. Gao, L. Wang, H. D. Nguyen, N. Kawamoto and T. Mori, *Adv. Funct. Mater.*, 2024, **34**, 2407017.
54 Z. Liu, W. Gao, H. Oshima, K. Nagase, C. H. Lee and T. Mori, *Nat. Commun.*, 2022, **13**, 1120.
55 J. W. Li, H. Gao, Z. Han, J. Yu, H. L. Zhuang, L. Chen, H. Li, Y. Jiang, Z. Wang, Q. Zheng and J. F. Li, *Adv. Mater.*, 2025, **37**, e2503665.
56 J. W. Li, Z. Han, J. Yu, H. L. Zhuang, H. Hu, B. Su, H. Li, Y. Jiang, L. Chen, W. Liu, Q. Zheng and J. F. Li, *Nat. Commun.*, 2023, **14**, 7428.
57 L. Wang, W. Zhang, S. Y. Back, N. Kawamoto, D. H. Nguyen and T. Mori, *Nat. Commun.*, 2024, **15**, 6800.
58 Z. Liu, N. Sato, W. Gao, K. Yubuta, N. Kawamoto, M. Mitome, K. Kurashima, Y. Owada, K. Nagase, C.-H. Lee, J. Yi, K. Tsuchiya and T. Mori, *Joule*, 2021, **5**, 1196–1208.

59 X. Chen, H. Wu, J. Cui, Y. Xiao, Y. Zhang, J. He, Y. Chen, J. Cao, W. Cai, S. J. Pennycook, Z. Liu, L.-D. Zhao and J. Sui, *Nano Energy*, 2018, **52**, 246–255.
60 J. W. Li, W. Liu, W. Xu, H. L. Zhuang, Z. Han, F. Jiang, P. Zhang, H. Hu, H. Gao, Y. Jiang, B. Cai, J. Pei, B. Su, Q. Li, K. Hayashi, H. Li, Y. Miyazaki, X. Cao, Q. Zheng and J. F. Li, *Adv. Mater.*, 2023, **35**, e2209119.
61 Q. Zhang, M. Yuan, K. Pang, Y. Zhang, R. Wang, X. Tan, G. Wu, H. Hu, J. Wu, P. Sun, G. Q. Liu and J. Jiang, *Adv. Mater.*, 2023, **35**, e2300338.
62 Y. K. Zhu, Y. Sun, J. Zhu, K. Song, Z. Liu, M. Liu, M. Guo, X. Dong, F. Guo, X. Tan, B. Yu, W. Cai, J. Jiang and J. Sui, *Small*, 2022, **18**, e2201352.
63 A. Nozariasbmarz, B. Poudel, W. Li, H. B. Kang, H. Zhu and S. Priya, *iScience*, 2020, **23**, 101340.
64 M. Jiang, Y. Fu, Q. Zhang, Z. Hu, A. Huang, S. Wang, L. Wang and W. Jiang, *Nat. Sci. Rev.*, 2023, **10**, nwad095.
65 X. Wu, Y. Lin, Z. Han, H. Li, C. Liu, Y. Wang, P. Zhang, K. Zhu, F. Jiang, J. Huang, H. Fan, F. Cheng, B. Ge and W. Liu, *Adv. Energy Mater.*, 2022, **12**, 2203039.
66 L. Yin, C. Chen, F. Zhang, X. Li, F. Bai, Z. Zhang, X. Wang, J. Mao, F. Cao, X. Chen, J. Sui, X. Liu and Q. Zhang, *Acta Mater.*, 2020, **198**, 25–34.
67 L. Wang, N. Sato, Y. Peng, R. Chetty, N. Kawamoto, D. H. Nguyen and T. Mori, *Adv. Energy Mater.*, 2023, **13**, 2301667.
68 J. Li, R. Chetty, Z. Liu, W. Gao and T. Mori, *Small*, 2025, **21**, e2408059.
69 X. Yang, H. Ni, X. Yu, B. Cao, J. Xing, Q. Chen, L. Xi, J. Liu, J. Zhang, K. Guo and J.-T. Zhao, *J. Materiomics*, 2024, **10**, 154–162.
70 J. Mao, H. S. Kim, J. Shuai, Z. Liu, R. He, U. Saparamadu, F. Tian, W. Liu and Z. Ren, *Acta Mater.*, 2016, **103**, 633–642.
71 L. Jiang, S. Tan, R. Chen, J. Xian, H. Li, D. Zhou, H. Kang, Z. Chen, E. Guo and T. Wang, *ACS Appl. Mater. Interfaces*, 2024, **16**, 60197–60207.
72 H.-S. Kim, Z. M. Gibbs, Y. Tang, H. Wang and G. J. Snyder, *APL Mater.*, 2015, **3**, 041506.
73 F. Zhang, C. Chen, H. Yao, F. Bai, L. Yin, X. Li, S. Li, W. Xue, Y. Wang, F. Cao, X. Liu, J. Sui and Q. Zhang, *Adv. Funct. Mater.*, 2019, **30**, 1906143.
74 L. Wang, A. Li, J. Li, N. Kawamoto, D. H. Nguyen and T. Mori, *Nano Energy*, 2025, **137**, 110797.
75 J. Callaway, *Phys. Rev.*, 1959, **113**, 1046–1051.
76 C. Xiong, F. Shi, H. Wang, J. Cai, S. Zhao, X. Tan, H. Hu, G. Liu, J. G. Noudem and J. Jiang, *ACS Appl. Mater. Interfaces*, 2021, **13**, 15429–15436.
77 R. Zhai, Y. Wu, T.-J. Zhu and X.-B. Zhao, *Cryst. Growth Des.*, 2018, **18**, 4646–4652.
78 J. Peng, D. Liu, S. Bai, Y. Wen, H. Liang, L. Su, X. Qian, D. Wang, X. Gao, Z. Ding, Q. Cao, Y. Pei, B. Qin and L. D. Zhao, *Adv. Energy Mater.*, 2025, **15**, 2404653.
79 N. Chen, H. Zhu, G. Li, Z. Fan, X. Zhang, J. Yang, T. Lu, Q. Liu, X. Wu, Y. Yao, Y. Shi and H. Zhao, *Nat. Commun.*, 2023, **14**, 4932.
80 X. Li, C. Chen, L. Yin, X. Wang, J. Mao, F. Cao and Q. Zhang, *Energy Environ. Sci.*, 2023, **16**, 6147–6154.
81 Y. Jiang, J. Dong, H. L. Zhuang, J. Yu, B. Su, H. Li, J. Pei, F. H. Sun, M. Zhou, H. Hu, J. W. Li, Z. Han, B. P. Zhang, T. Mori and J. F. Li, *Nat. Commun.*, 2022, **13**, 6087.
82 J. Zhou, Z. Chen, J. Luo, W. Li and Y. Pei, *Adv. Mater.*, 2024, **36**, e2405299.
83 Y. Qin, B. Qin, T. Hong, X. Zhang, D. Wang, D. Liu, Z. Y. Wang, L. Su, S. Wang, X. Gao, Z. H. Ge and L. D. Zhao, *Science*, 2024, **383**, 1204–1209.
84 Y. Zhang, Z. Li, S. Singh, A. Nozariasbmarz, W. Li, A. Genc, Y. Xia, L. Zheng, S. H. Lee, S. K. Karan, G. K. Goyal, N. Liu, S. M. Mohan, Z. Mao, A. Cabot, C. Wolverton, B. Poudel and S. Priya, *Adv. Mater.*, 2023, **35**, e2208994.
85 D. Liu, S. Bai, Y. Tian, J. Peng, S. Liu, H. Shi, H. Liang, Y. Qin, L. Su, X. Qian, B. Qin and L. D. Zhao, *Adv. Mater.*, 2025, **37**, e2506999.
86 M. T. Agne, K. Imasato, S. Anand, K. Lee, S. K. Bux, A. Zevalkink, A. J. E. Rettie, D. Y. Chung, M. G. Kanatzidis and G. J. Snyder, *Mater. Today Phys.*, 2018, **6**, 83–88.

